Supramolecular Self-Assembly and Radical Kinetics in Conducting Self-Replicating Nanowires

Irina Nyrkova,[†,∥] Emilie Moulin,[†,∥] Joseph J. Armao, IV,[†] Mounir Maaloum,[†] Benoît Heinrich,[§] Michel Rawiso,[†] Frédéric Niess,[†] Juan-Jose Cid,[†] Nicolas Jouault,[‡] Eric Buhler,[‡] Alexander N. Semenov,[*,†] and Nicolas Giuseppone[*,†,⊥]

[†]Institut Charles Sadron, CNRS, 23 rue du Loess, BP 84047, 67034 Strasbourg Cedex 2, France, [‡]Matière et Systèmes Complexes (MSC) Laboratory, University of Paris Diderot—Paris VII, 75205 Paris Cedex 13, France, [§]Institut de Physique et Chimie des Matériaux de Strasbourg, 23 rue du Loess, BP 43, 67034 Strasbourg Cedex 2, France, and [⊥]Department of Chemistry, University of Strasbourg, 67000 Strasbourg, France. [∥]I.N. and E.M. contributed equally to this work.

ABSTRACT By using a combination of experimental and theoretical tools, we elucidate unique physical characteristics of supramolecular triarylamine nanowires (STANWs), their packed structure, as well as the entire kinetics of the associated radical-controlled supramolecular polymerization process. AFM, small-angle X-ray scattering, and all-atomic computer modeling reveal the two-columnar "snowflake" internal structure of the fibers involving the π-stacking of triarylamines with alternating handedness. The polymerization process and the kinetics of triarylammonium radicals formation and decay are studied by UV—vis spectroscopy, nuclear magnetic resonance and electronic paramagnetic resonance. We fully describe these experimental data with theoretical models demonstrating that the supramolecular self-assembly starts by the production of radicals that are required for nucleation of double-columnar fibrils followed by their growth in double-strand filaments. We also elucidate nontrivial kinetics of this self-assembly process revealing sigmoid time dependency and complex self-replicating behavior. The hierarchical approach and other ideas proposed here provide a general tool to study kinetics in a large number of self-assembling fibrillar systems.

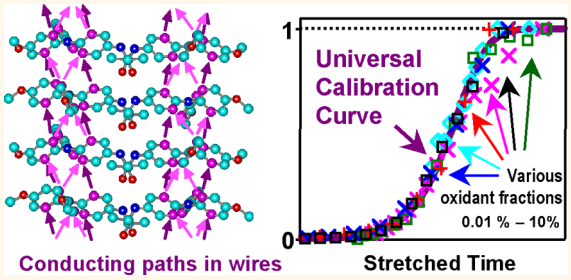

KEYWORDS: supramolecular polymers · fibrils · self-replication · triarylamines · light-triggered self-assembly

Molecular self-assembly represents a powerful bottom-up approach to build nanoscaled functional materials.[1,2] It rests on the autonomous organization of molecular components defined by their shape, charge, polarizability, *etc.* and takes advantage of kinetically labile supramolecular bonds to interact and produce systems of increasing complexity.[3−6] This intrinsic supramolecular mobility leads to ordered nanostructures upon equilibration between aggregated and nonaggregated states, thus providing a number of interesting properties such as error correction, self-healing, and high sensitivity to external stimuli.[7,8]

The resulting soft materials are typically characterized by multiscaled organization based on hierarchically arranged *mesostructures*.[9−12] Their distinctive feature is a *limited disorder*: the structures are well-ordered at a microscale, but, because of symmetry conflicts or kinetic reasons, are organized differently at larger length-scales. Understanding of correlations between the chemical structure of the primary molecular constituents and the protocol of system preparation on one side, and the resulting hierarchical organization and its macroscopic characteristics on the other side, is a challenging and rarely feasible task.[13−16]

The extreme complexity of such soft materials prohibits direct simulation of their properties starting from the atomistic level.[17] However, one can adopt a different approach involving target-oriented experiments combined with *hierarchical analysis*[18,19] of the system including (1) atomistic simulations at short scales, (2) statistical physics methods at mesoscales and (3) materials physics models at macroscale. This approach is used here to study self-organization of chemically tailored derivatives of triarylamines (TAA) capable to fibrillize upon simple

* Address correspondence to semenov@unistra.fr, giuseppone@unistra.fr.

Received for review May 26, 2014 and accepted September 20, 2014.

Published online September 21, 2014
10.1021/nn502863b

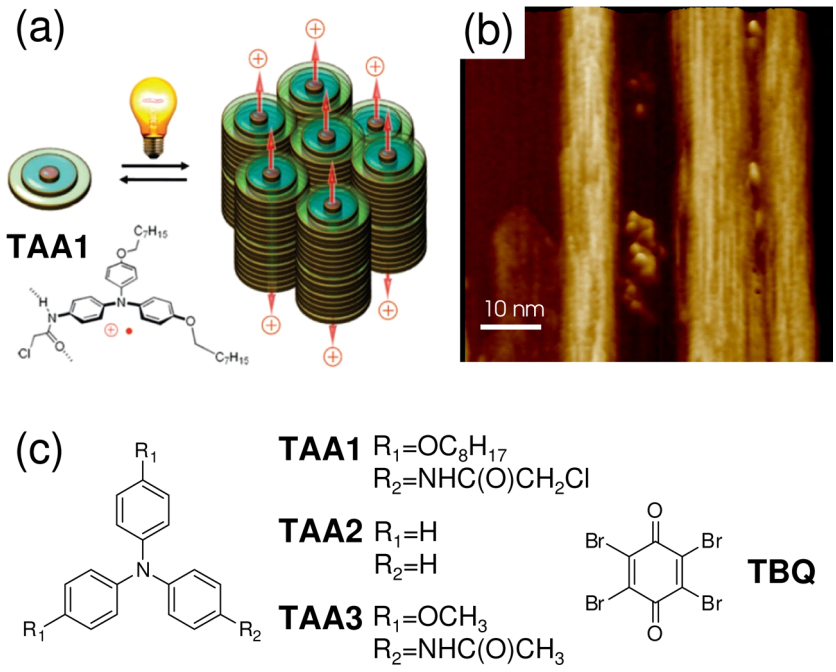

Figure 1. (a) Schematic representation of the supramolecular self-assembly obtained from an amide-modified triarylamine upon light irradiation. (b) The corresponding AFM image of the self-assembled fiber. (c) The amine molecules used in experiments (TAA1) and in modeling (TAA2, TAA3) and (d) the oxidant TBQ.

exposure to visible light producing highly conductive supramolecular triarylamine nanowires (STANWs), Figure 1.[20,21] In particular, we explore in detail the hypothesis that this structuring process can occur as a result of highly intriguing synergistic phenomena that start with the light-induced formation of triarylammonium cationic radicals.

More generally, we explore three alternative ways of provoking the fibrillization from initially stable monomeric **TAA1** solutions: (a) by light exposure, (b) by chemical oxidation and (c) by seeding with similar fibril fragments. The characteristic sigmoid self-replicating curves and surprisingly long memory effects are registered in all the cases. To elucidate these effects, we perform detailed structural and kinetic analysis of model TAA systems, establish the underlying autocatalytic reactions and obtain their main parameters. In particular, we uncover the stimuli-induced multistage mechanisms of the radical-controlled TAA polymerization and predict quantitatively the long-time kinetics and stability of radicals in excellent agreement with EPR data. These goals are achieved by combining experimental techniques, atomistic simulations and continuum statistical and kinetic models.

The properties and performance of functional self-assembling organic materials are defined by their molecular organization. Here we deal with such complex organization involving both neutral TAA molecules and their cationic radicals forming columnar aggregates. We performed extensive atomistic simulations revealing their full structure, which is shown to be in agreement with AFM and XRD experimental data. It turns out that the radicals can aggregate with themselves and with neutral triarylamines by charge transfer in conjunction with hydrogen bonding, $\pi-\pi$ stacking, dipole−dipole and van der Waals interactions. This coalition of interactions leads to formation of molecular *double "snowflake"* wires, which can combine into very strongly packed bundles of larger and stiffer fibers.

The light-induced aggregation is marked by drastic changes of the ^{1}H NMR spectra and of the solution color attributed both to the presence of the radicals and to the structuring. The radical-controlled TAA self-assembly yielding very stable fibers can be controlled by a combination of light and electric field triggers.[22,23] It has been used for spatially precise interconnection of electrodes producing outstanding conductivity of metallic character.[24,25] As we show below, it is likely that this high charge conduction is related to the natural presence of cationic radicals stabilized in the fibrils and providing its autodoping. Importantly, the obtained interatomic distances between the neighboring stacked molecules are compatible with continuous pathways of overlapping π-orbitals allowing an efficient charge transfer along the nanowires. Therefore, the present detailed study regarding the radical content, the ways to control it in STANWs, and other results could facilitate construction of advanced functional and dynamic electroactive materials.

RESULTS AND DISCUSSION

Autocatalytic Self-Replication of Fibrils: Initiation and Kinetics. A solution of **TAA1** in chloroform is light-yellow right after

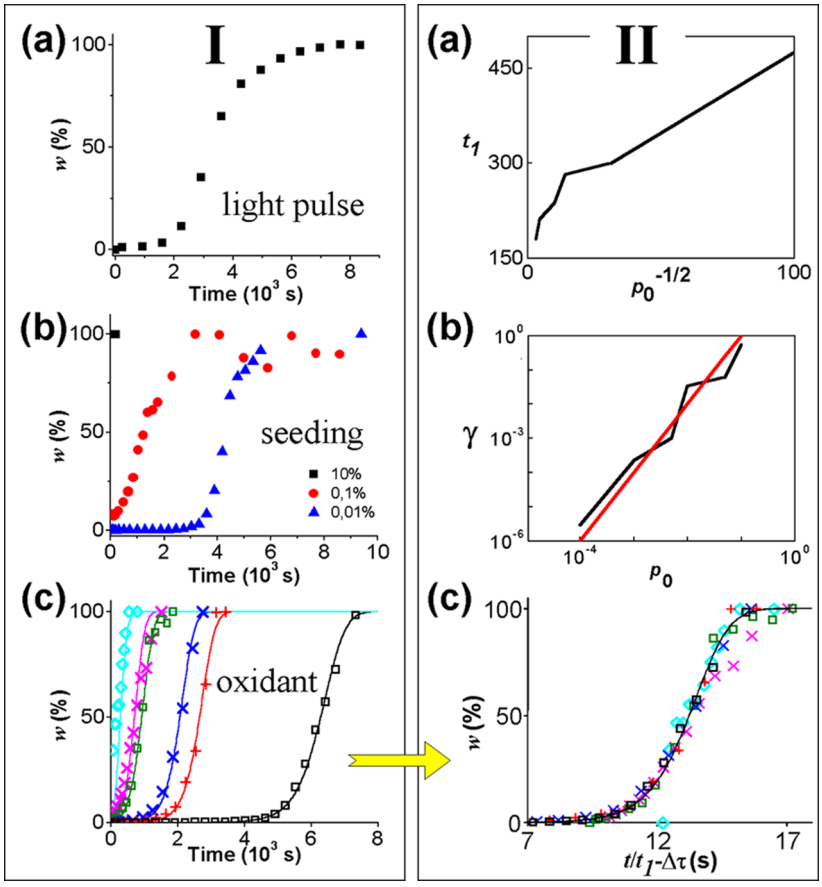

Figure 2. Autocatalytic fibrillization of TAA in chloroform solutions. (I) Time-resolved NMR data on the fraction *w* of self-assembled TAA1 molecules in $CDCl_3$: (a) *w vs* time *t* in a fresh solution (c_A = 10 mM) after a short (1 s) light pulse at *t* = 0. (b) The data on aggregation in a nonirradiated fresh solutions (c_A = 1 mM) initiated by "seeding" with 10, 0.1 and 0.01% of irradiated molecules added at *t* = 0. (c) *w vs t* for TAA1 solutions (c_A = 10 mM) prepared with added TBQ oxidant and the theory curves (t_1 and γ are treated as the fitting parameters for each curve). Oxidant molar fractions are (from the left to the right) p_O = 10, 5, 1, 0.5, 0.1, 0.01%. (II) Analysis of the TBQ-induced fibrillization data from the panel Ic: (a) The characteristic fibril growth time t_1 *vs* $p_O^{-1/2}$, where $p_O = c_O/c_A$ is the relative concentration of the oxidant. (b) The dependence of the reduced nucleation rate γ on p_O deduced from the NMR data (black curve); the theoretical dependence for *n* = 3 (red line). (c) The degree of aggregation *w vs* reduced time $t/t_1 - \Delta\tau$. The NMR data (symbols as in (Ic)) are compared with the master theory curve, eq 5 with const$_\tau \approx -12.8$ (black solid).

purification. It proved stable for a long time if kept in the dark in the absence of oxidation. However, when exposed to visible white light for a few minutes, it changes color to light-green. This transition is marked by a full disappearance of the NMR signal from the aromatic, aliphatic ether and acetamide protons, while the main aliphatic chain signal remains intact. These changes persist for a few weeks in the dark and are attributed to the self-assembly of TAA (see section SI.2 in the Supporting Information, SI), which thus can be conveniently monitored by NMR.[20]

The aggregation process turns out to be very fast in the case of light exposure for more than 5 s: in this case, the first NMR spectrum already shows a complete transformation from monomeric resonance signals to those characteristic of the aggregated state. Interestingly, the situation is different with a short irradiation pulse, which has a long-time impact on the solution: Upon just 1 s of irradiation, no noticeable change occurs during the first 15−20 min. The aggregation then starts in the **TAA1** solution and it finally transforms into the fully aggregated state in about 2 h (Figure 2.Ia). The self-assembly curve thus shows a sigmoid shape, which is typical for an autocatalytic process.

Similar sigmoid aggregation curves are produced on addition of catalytic quantities of chemical oxidant, or when the solution was "seeded" with an already fibrillized **TAA1** material, Figure 2.Ib,c. These observations confirm the idea that while the presence of radicals may trigger the aggregation, the fibrils in **TAA1** solutions are absolutely stable thermodynamically even in the absence of radicals.

We show below that the aggregation curves Figure 2.I are a valuable source of information on the kinetic pathways and the final self-assembled structure. For the first illustration we choose the case of the oxidant trigger, 2,3,5,6-tetrabromobenzoquinone (**TBQ**) (Figure 2.Ic). Indeed, this additive strongly oxidizes TAA producing the radicals, $TAA^{\bullet+}$ and $\mathbf{TBQ}^{\bullet-}$. The reverse reaction is suppressed energetically and can be neglected. Therefore,

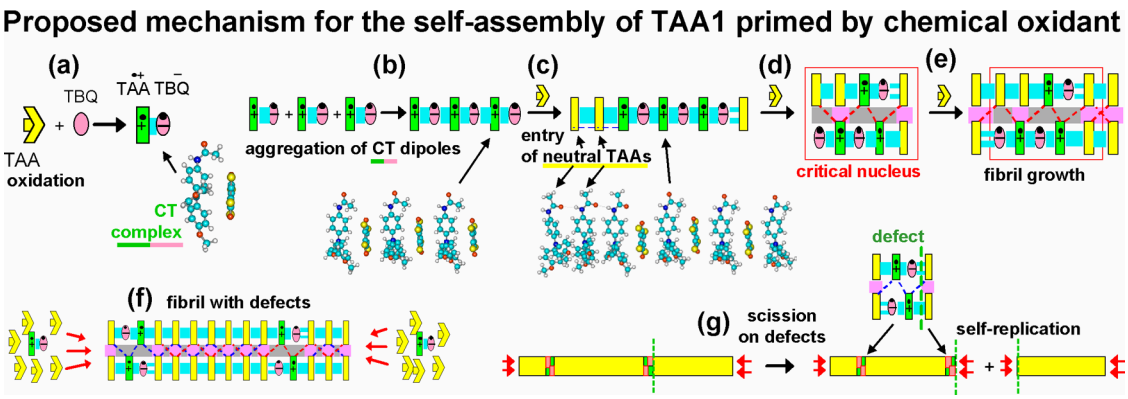

Figure 3. Oxidant-induced aggregation kinetics in TAA solutions: (a) Oxidation of monomeric TAA by TBQ produces the radical ion pair $TAA^{\bullet+}TBQ^{\bullet-}$. (b–g) The main stages of the critical nuclei formation and subsequent fibril multiplication in TAA solutions with added TBQ: (b) Association of $TAA^{\bullet+}TBQ^{\bullet-}$ ion pairs. (c) End-attachment of neutral TAA molecules. (d) The critical nucleus formation with $n = 3$ $TAA^{\bullet+}$ radicals, and (e,f) further growth of the bicolumnar fibril by end-attachment of free amines. (g) Self-replication by scission at defect points.

the number of radical amines must be nearly equal to the number of oxidant molecules.

The early stages of aggregation are studied by all-atomic calculations based on **TAA3** model shortcut molecules (see section SI.8 in the SI). The radicals $TAA^{\bullet+}$ and oxidant anions form stable charge-transfer (CT) complexes $TAA^{\bullet+}TBQ^{\bullet-}$ (Figure 3a) with high dissociation energy, $E_{ca} \approx 58k_BT$, meaning that in practice the dissociation is prohibited.[26,27] Being electric dipoles, the charge-transfer complexes can effectively assemble in supramolecular stacks: the scission energy stabilizing these stacks is $\approx 28k_BT$ for dimers and $\approx 31k_BT$ for long stacks (Figure 3b). Moreover, the initial cation–anion columns attract neutral TAAs at their ends *via* aromatic stacking and H-bond interactions (Figure 3c). The long enough single columns eventually form double columnar (DC) structures (Figure 3d) stabilized mainly by the intercolumnar H-bonding and side-to-side van der Waals attractions (the lateral attraction energy gain is $\approx 14k_BT$ per neutral TAA molecule involved in the H-bonding). The DC aggregates are very stable: they can effectively trap new TAA molecules at their ends (the corresponding energy gain is $E_{as}^{(2)} \approx 18k_BT$)[27] serving as *nuclei* for the further end-growth of the fibrils, Figure 3e. As long as free $TAA^{\bullet+}$**TBQ**$^{\bullet-}$ complexes are still present in the solution, they can also enter into the growing fibrils producing *defects*, which are weak points in the fibril structure (see Figure 3f). On a long time scale it tends to break at a defect (see Figure 3g);[28] the fibril scission energies are ≈ 55 and $\approx 41k_BT$, respectively, for the regular double stack and for a defect point (corresponding to $\sim 10^6$ times higher probability to break at a defect).

The kinetics of this multistage self-assembly process can be described in terms of two basic quantities: the number of fibrils $m = m(t)$ and the total number of aggregated amines $M = M(t)$. If c_A and c_O are the total molar concentrations of TAA and **TBQ** in solution ($p_O \equiv c_O/c_A$ is the oxidant fraction, which is supposed to be low), and c, c_+ are concentrations of free TAA molecules and of free cation–anion complexes, respectively, then $c+M = c_A$; $c_+ \approx cp_O$. The kinetic equations are

$$\frac{dM}{dt} = k(c - c^*)m, \quad \frac{dm}{dt} = \lambda M p_O + \Gamma_n \qquad (1)$$

Here kc is the rate of association of dissolved TAA molecules at a fibril end and kc^* = const is the fibril dissociation rate, which is neglected hereafter since the critical association concentration c^* is extremely low: $c^* \ll c_A$ (see the next section). The λ-term in the second equation accounts for the formation of new fibrils by scission at the defects (Mp_O is the total number of radical-defects in the fibrils), $\Gamma_n = k'c_+^n c^\nu$ is the fibril nucleation rate, and k, k' and λ are the relevant rate constants (the critical nucleus $(TAA^{\bullet+})_nTAA_\nu$ is assumed to involve both radical cations and neutral amines, *cf.* Figure 3d).

The phenomenon of fibril *self-replication* is pronounced if the initial nucleation rate $\Gamma_n \approx k'p_O^n c_A^{n+\nu}$ is much lower than the maximum scission rate $\lambda c_A p_O$:

$$\gamma \ll 1, \quad \gamma \equiv \Gamma_n/(\lambda c_A p_O) \approx (k'/\lambda)p_O^{n-1}c_A^{n+\nu-1} \qquad (2)$$

In this case the self-assembly in accordance with eq 1 follows the universal curve:

$$w \simeq 1 - \exp(-\mu), \quad \tau = \operatorname{arcosh}(1 + \mu/\gamma) + \varphi(\mu) \qquad (3)$$

where the weight fraction of the aggregated amines $w \equiv M/c_A$ and the reduced time

$$\tau \equiv t/t_1, \quad t_1 = (k\lambda p_O c_A)^{-1/2} \qquad (4)$$

are related implicitly *via* an auxiliary variable μ and the universal function $\varphi(\mu)$:

$$\varphi(\mu) = \int_0^\mu \left(\frac{1}{\sqrt{2}\sqrt{\mu + \exp(-\mu) - 1}} - \frac{1}{\mu} \right) d\mu$$

This model reproduces very well (with fitted t_1 and γ) all the experimental NMR data on the kinetics

of the TAA aggregation for various oxidant concentrations, p_O (*cf.* Figure 2.Ic).

The dependence of the obtained growth time t_1 on the oxidant concentration p_O is shown in Figure 2.IIa. We plot $p_O^{-1/2}$ along the horizontal axis as our theory predicts that $t_1 \propto p_O^{-1/2}$. The plot shows that t_1 is indeed nearly linear in $p_O^{-1/2}$. However, the experimental dependence t_1 *vs* p_O is weaker than the theoretical prediction. In particular, it seems that t_1 tends to a finite constant rather than to 0 at high p_O. This deviation is expected since the theory is valid for small $\gamma \ll 1$, while this condition is violated at high p_O (see Figure 2.IIb). The latter regime corresponds to a high nucleation rate, $\gamma \gtrsim 0.1$, when the self-replication of fibrils is less important and the dependence of t_1 on p_O becomes weaker. A similar effect is also expected at very low $p_O \lesssim 10^{-5}$: in this regime the homogeneous scission of fibrils is competitive with the scission at the extremely rare defects associated with the radicals.

The dependence of the parameter γ on p_O is shown in Figure 2.IIb. It is obvious that it is close to $\gamma \propto p_O^2$, which points to $n = 3$, eq 2. We thus deduce that the critical nucleus in the systems with **TBQ** oxidant should typically involve $n = 3$ radical cations ($TAA^{\bullet+}$).

To perform a more detailed comparison, we note that the theoretical curves $w(\tau)$ eq 3 for various γ have nearly the same shape as long as $\gamma \ll 1$: the curves are simply shifted one with respect to another along τ giving the universal dependence

$$w = w_{\text{univ}}(\tau - \Delta\tau), \text{ with } \Delta\tau = \text{const}_\tau - \ln\gamma \quad (5)$$

where $w_{\text{univ}}(\tau)$ is a universal function, independent of any material constant. Therefore, we predict an essentially universal growth of the aggregated fraction w in terms of the appropriate time parameter $\tilde{\tau} = t/t_1 - \Delta\tau$ (*i.e.*, with appropriately shifted and rescaled time). In other words, the fibril growth time t_1 is nearly independent of γ; it is just the lag-time before the growth that crucially depends on the nucleation rate, $t_{\text{delay}} \simeq t_1 \ln 1/\gamma$. The master curve representation, eq 5, of the NMR data is shown in Figure 2.IIc.

Finally, returning to the system without oxidant, we note that the same kinetic mechanism (fibril end-growth + scission) can explain the kinetics of TAA self-assembly in pure chloroform solutions triggered by a short pulse of light, or, alternatively, by a small amount of added fibril "seeds" (*cf.* Figure 2.Ia,b). In this case, both the scission rate and the end-growth rate constants are independent of the irradiation dose I, or of the amount of seeds, c_s. The TAA self-assembly in these systems can be described by the same eq 1, but with Γ_n replaced by const $\times \delta(t)$ (here const $\propto I, c_s$ and δ is the Dirac's delta), and λp_O replaced with the homogeneous scission rate constant λ_h. Therefore, the characteristic aggregation time t_1, eq 4, is predicted to be constant (independent of I or c_s) and similar to the time t_1 for low oxidant fraction p_O, in agreement with the NMR kinetic data giving $t_1 \sim (2 \div 3)\cdot 10^3$ s (*cf.* Figure 2.Ia,b). By contrast, c_s still defines the delay time for the seeded systems (*cf.* Figure 2.Ib).

Photoinduced TAA Aggregation: Nucleation and Structure. Almost perfect fibrillar TAA structures, Figure 4.I, were produced by long-time white-light irradiation of freshly prepared solutions of monomeric TAA in chloroform. The UV spectra taken in the course of the irradiation (Figure 5a) show a slow growth of new absorption bands indicating production of triarylammonium radicals,[29] **TAA**$^{\bullet+}$. The formation of the radicals is also directly confirmed by the time-resolved EPR data (see Figure 5a,b). The radicals therefore seem to be a prerequisite for aggregation as it was never observed in those solvents that do not allow for photooxidation of TAA (see section SI.3 in SI). A solvent with sufficient oxidizing ability (like chloroform) is thus indispensable for the self-assembly, although the solvent itself does not induce chemical oxidation of the TAA in the dark.

The principal early stages of the light-induced aggregation can be elucidated by all-atomic simulations of model **TAA2** and **TAA3** molecules Figure 1c (see section SI.8). The key elements defining the stacking ability of TAA molecules are their conformation and charge distribution. Our quantum mechanics analysis demonstrates a major geometrical change associated with the TAA radical formation: The neutral TAA molecules adopt a pyramidal conformation with strong out-of-plane rotation of the aromatic rings. However, the TAA amine pyramid becomes flat and the ring rotation angles decrease significantly after oxidation. The flat TAA radicals facilitate stacking, in agreement with the experimental evidence that the association of TAA molecules in solution is correlated with the TAA radical cation formation.

The basic reaction stages of this light-induced oxidation process are[30] (Figure 4.IIb):

$$TAA \xrightarrow{h\nu} TAA* \quad (6)$$

$$TAA* + CHCl_3 \rightarrow TAA^{\bullet+} + Cl^- + CHCl_2^{\bullet} \quad (7)$$

and for reduction (Figure 6.II):

$$2(TAA^{\bullet+} + Cl^-) \rightarrow 2TAA + Cl_2 \quad (8)$$

Noteworthy, $TAA^{\bullet+}$ and Cl^- ions form a rather stable cation−anion complex. The ion-bond energy, E_{ca}, obtained by the simulation technique is $E_{ca} \approx 55 k_B T$. This energy is high enough to practically suppress the dissociation: the fraction of dissociated radicals is about $e^{-E_{ca}/2k_BT} \sim 10^{-12}$.

$TAA^{\bullet+}Cl^-$ ion pairs are electric dipoles that can effectively assemble in supramolecular stacks. The optimal configuration of the stack depends on the number of $TAA^{\bullet+}Cl^-$ pairs in it (see Figure 4.IIc−i). Formation of the supramolecular pile of dipoles starts with association of just two cation−anion pairs, the attraction energy stabilizing such dimers (Figure 4.IId) is $E_{11} \approx 15.5 k_B T$. The energy gain for end-attachment of

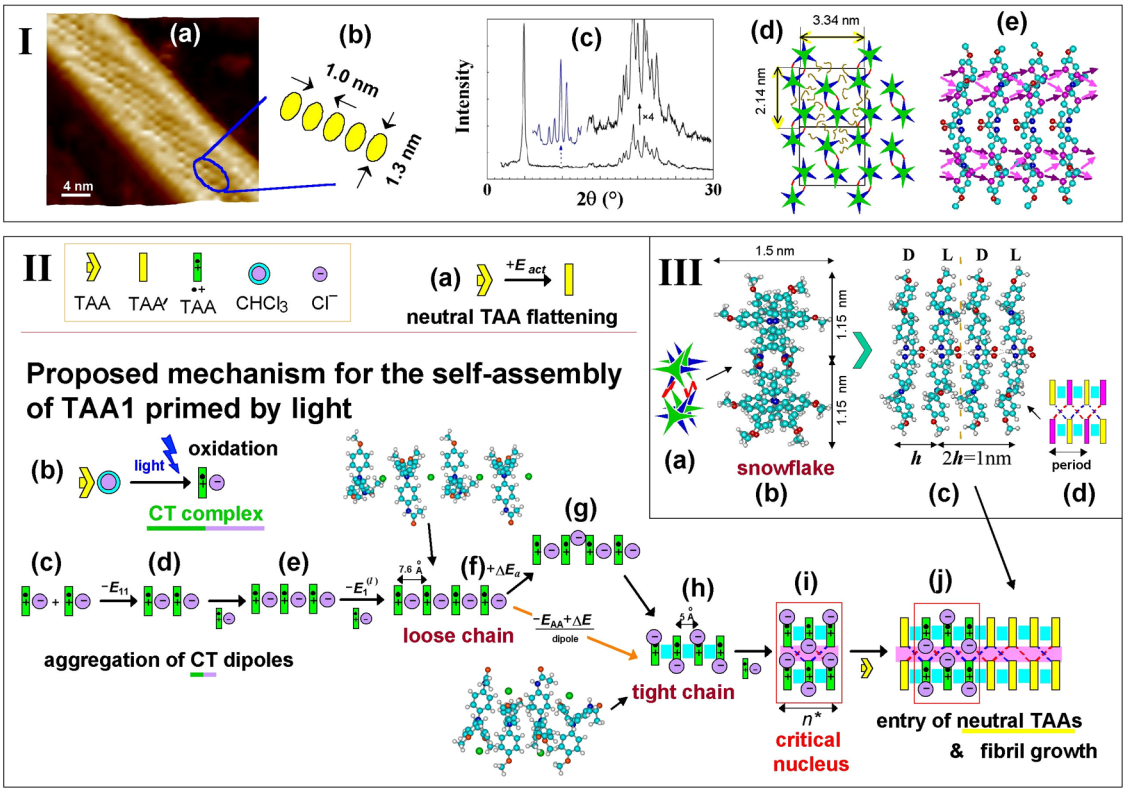

Figure 4. TAA fibrils in chloroform after 1 h exposition to white light. (I) (a,b) AFM height image (dry phase) of maize-like structures formed in 1 mM solution of TAA1 in chloroform. (c) The original XRD pattern from 10 mM TAA1 sample (bottom, black) accompanied by its magnification in the WAXS range (top, black) and in the SAXS range (top, blue) registered on the high-flux line. (d) The proposed internal molecular organization of TAA1 fibrils (in the plane normal to the c-axis) based on the XRD: the lattice cells are shown by rectangles; each crystalline cell consists of 8 molecules and includes two layers (TAA molecules belonging to different layers are shown with green and blue colors, respectively). Amide bonds are shown with red segments, and alkyl side chains with brown curly lines. (e) The simulated all-atomic structure of snowflake double column: the conducting pathways formed between nearest-neighboring carbons (marked with violet color) of adjacent TAA molecules (R_{CC} = 0.36−0.37 nm) are marked with violet arrows (hydrogens are not shown). (II) Light-induced aggregation kinetics in TAA solutions. (a) Highly improbable spontaneous flattening of isolated neutral TAA molecule (transition TAA → TAA′). (b) Light induces oxidation of a neutral TAA molecule producing $TAA^{\bullet+}$ radical and Cl^- anion. (c,d) Two free radicals $TAA^{\bullet+}$ complexed with the Cl^- counterions attract each other head-to-tail. (e,f) A growing stack of radical dipoles. (f,g,h) Tightening of the stack: chloride ions move sideways (g); aromatic rings of TAA molecules benefit from closer contacts, while chloride anions are finally accommodated in the gaps between ether tails of TAA molecules (h). (i) Formation of double-columnar nuclei stabilized by H-bonds between the columns. (j) Growth of the structure by attachment of neutral TAA molecules. (III) Molecular arrangements in bicolumnar "snowflake" stacks of neutral TAA3: (a) A cartoon showing alternating molecular orientation in the columns. (b) The top view (along the main axis), and (c) the side view of the structure. (d) A cartoon with zigzag chain of H-bonds connecting the columns.

a dipole to a long stack of dipoles is even higher: $\tilde{E}_1^{(l)} \approx 16.5k_BT$ (Figure 4.IIf). Hence, the dimers associate readily if their concentration is above $\sim 10^{-7}$ M.

Simulations suggest two principal arrangements of $TAA^{\bullet+}Cl^-$ pairs in long supramolecular stacks: a *loose* chain with symmetrically positioned chlorides (Figure 4.IIf), and a *tight* chain with chloride counterions in the off-axis positions (Figure 4.IIh), the latter being much more stable (as direct contacts between neighboring TAAs allow for their correct π-stacking and optimal van-der-Waals attraction). Indeed, the scission energy of the tight stack, $\tilde{E}_{sc}$, is higher by $\approx 12.7k_BT$ and its overall association energy (per charge-transfer complex) $\tilde{E}_1$ is stronger by $\approx 6.7k_BT$ in comparison with the values for the loose chain. However, a transformation from the "loose" to the more favored "tight" structure demands multiple rearrangements (Figure 4.IIg) of chloride ions. The corresponding activation energy is on the order of $\Delta E_a \sim 8.6k_BT$. Such transformation is only possible for chains longer than a trimer since an isolated "tight" dimer is less favorable than a "loose" dimer (while the energies of the corresponding trimers are roughly the same).

Long aggregates of $TAA^{\bullet+}Cl^-$ pairs tend to form double columns stabilized by significant lateral attraction energy (including the H-bond energy). The minimal stable double-columnar aggregate involves $n^* \sim 3$ charge-transfer pairs per column (Figure 4.IIi). Its energy is lower by $\sim 15 \pm 5\ k_BT$ than that of a single-columnar "tight" stack of $2n^*$ dipoles.

Once a double-columnar nucleus (Figure 4.IIi) is formed, it attracts neutral TAA molecules that attach at its ends by aromatic stacking and H-bonding, thus initiating proliferation of TAA aggregation without

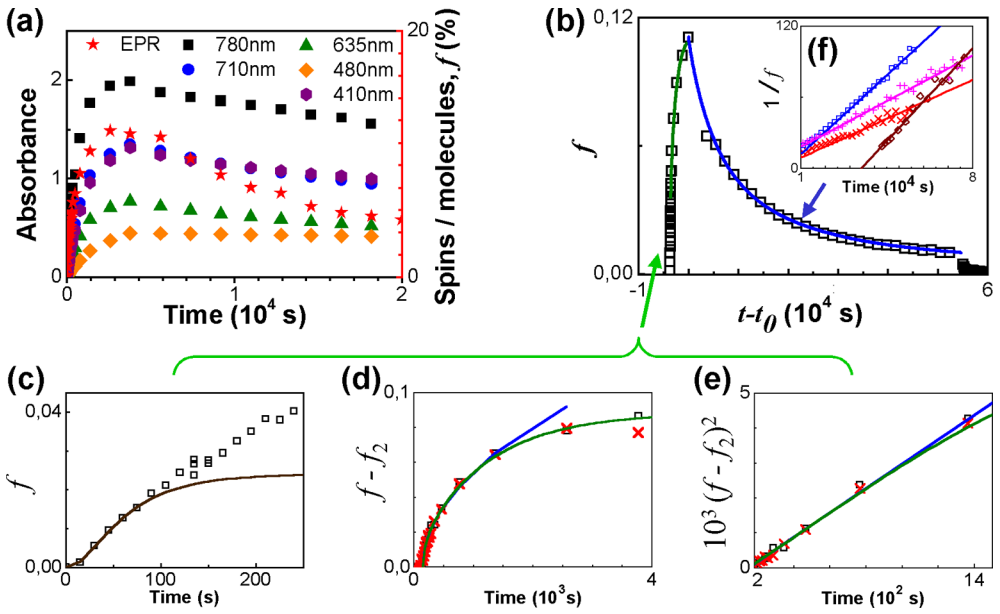

Figure 5. Kinetics of light-induced radical formation and decay in the dark. (a) Time evolution of the UV absorbance at 5 different wavelengths and of the fraction f of the triarylammonium radical (quantitative EPR data) for TAA1 solutions in chloroform (at 1 mM) during both 1 h irradiation ($I = 0.06 W/cm^2$) and overnight relaxation in the dark. (b) Time dependence of the number fraction of radicals, f *vs* $t - t_0$ for 10 mM TAA solution irradiated for 1 h at $t < t_0 = 3765$ s: EPR data (squares) and theoretical curves in accordance with eqs 23, 26 (blue curve for $t > t_0$) and with eq 22 (green curve for $t < t_0$ corresponds to the green curve in graph (d)). The fraction of radicals at the beginning of the dark stage $\rho_0 = f(t_0) \approx 0.111$; the solution was heated up at $t > 62000$ s. (c–e): Radical formation in solutions of initially monomeric TAA1 during 1 h irradiation stage ($I = 0.06 W/cm^2$) in chloroform: EPR data for the fraction of radicals, f *vs* t at $c_A = 10$ mM (black squares) and at $c_A = 1$ mM (red crosses). The solid curves comes from the theory with $f_2 = 0.024$ ($c_A = 10$ mM) and $f_2 = 0.032$ ($c_A = 1$ mM). (c) The early stage data and the theory according to eq 18 with $n^* = 3$, $t_c = 60$ s (brown curve) for $c_A = 10$ mM. (d) The excess relative number of radicals, $f - f_2$ *vs* t: the theory, eq 22, with $p_e - f_2 = 0.088$, $t_m = 1150$ s and $t_f = 150$ s (green curve); the corresponding theoretical asymptote, $f - f_2 = 0.00187((t - t_f)/s)^{1/2}$ (blue curve). (e) The same data and the theoretical curves from (d) for the time range $t = 150 \div 1500$ s: the square of the excess radical amount, $(f - f_2)^2$, *vs* t. (f) Radical decay in the dark after 1 h of irradiation: $1/f$ *vs* t. EPR data sets (symbols) and the corresponding linear regression approximations for $t > 2 \times 10^4$ s (solid lines, eq 25) for $c_A = 10$ mM (blue, data as in the plot (b)), 1 mM (two independent experiments, red (the data as in the plot (a)) and magenta), and for another solution, $c_A = 1$ mM, sonicated in the dark (brown, the data of the experiment of Figure 7a); in the latter case the experimental time is multiplied by 10 for better visibility.

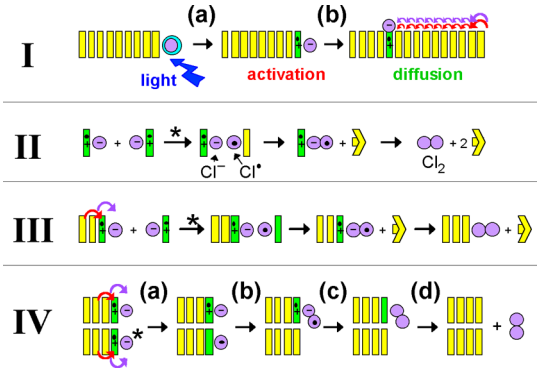

Figure 6. (I) Photo-oxidation of a TAA molecule at a fibril end (a) followed by diffusion of the new-born cation–anion pair inside the fibril (b). The chloride anion moves physically (see violet arrows), the TAA radical diffuses *via* electronic exchange with neighboring neutral TAA molecules (red arrows). (II) Pairwise annihilation of two free cation–anion complexes, eq 8. (III) Annihilation of a radical at the end of a fibril aided by a free radical (see the text above eq 20). (IV) Self-assisted reduction of two radicals at the end of a two-columnar fibril.

any further molecular oxidation (Figure 4.IIj). The total energy gained when a neutral TAA molecule enters the most energetically favorable double-columnar "snowflake" TAA fibril (Figure 4.III) is $E_{as}^{(2)} \approx 18 k_B T$;[27] it corresponds to an extremely low critical association concentration $c^* \sim 10^{-8}$ M. Therefore, practically all TAA molecules should eventually aggregate. On the other hand, the activation energy to transform a free TAA molecule into the association-ready state TAA′ (flat and solvent-dissociated) is high, $E_{act} \approx 16 k_B T$ (Figure 4.IIa), so neutral TAAs cannot start the self-assembly on their own, hence a nucleus formed by radicals is required for that (otherwise, at least eight activated neutral molecules are needed to nucleate a fibril leading to a prohibitive energy barrier of $\sim 128 k_B T$).

In accordance with our all-atomic simulations based on **TAA3** shortcut molecules (section SI.8 in SI), the TAA fibril structure involves the "snowflake" double columnar arrangement, Figure 4.III (another single columnar structure, called "Mercedes-Benz", is less favorable: its energy is higher by $\sim 5 k_B T$ per TAA). While isolated neutral TAA has a pyramidal conformation with strong out-of-plane rotation of rings, the molecule adopts "propeller-like" conformation TAA′ after entering the stack: the pyramid becomes flat and the ring rotation

angles decrease. Two chiral geometries (L, D) are possible depending on the propeller twirl sense. In each single snowflake column, the twirl sense alternate (see Figure 4.IIIa,c), so the aryl rings from neighboring TAA molecules closely approach each other. The amide groups facilitate stacking by intercolumnar H-bonds forming the double-columnar pattern (see Figure 4.IIIc,d). The primitive crystalline lattice cell for the double-columnar "snowflake" structure thus corresponds to at least 4 TAA molecules (the dashed brown line in Figure 4.IIIc separates the structure in two such cells).

This picture is confirmed by the AFM images revealing that **TAA1** molecules form the characteristic maize-like aggregates, their main motif being based on the columnar arrangement of "grains" of *ca*. 1.3 nm diameter, with in-columnar period of *ca*. 1.0 nm, Figure 4. Ia,b. These parameters are consistent with the "snowflake" morphology (Figure 4.IIIb,c) obtained by simulations of the model **TAA3** molecules: the sizes of one "snowflake" are ≈1.5 and ≈1.15 nm in two directions perpendicular to the main axis, and the LD-period along the column is $2h$ = 1.0 nm.[31]

An analysis of X-ray diffractograms (Figure 4.Ic) from self-assembled structures of **TAA1** in chloroform yields on its own the possibility of 2 slightly different atomic arrangements corresponding to the same 2D lattice in the reciprocal space, which is well-characterized by a large number of well-resolved (*hk*0) reflections. Both atomic arrangements point to monoclinic cells of $Z = 8$ molecules. The columns are oriented along the monoclinic **c** vector with the lattice parameter of 1.00 or 1.05 nm, and are arranged laterally in a rectangular 3.34 nm × 2.14 nm sublattice, as shown in Figure 4.Id (see section SI.5 in the SI for details). These lattice periods agree very well with the main period ($2h$ = 1.0 nm), the width (2.3 nm) and the double depth (1.5 nm × 2) of the double-columnar snowflake aggregates yielded by simulations (Figure 4.III). Moreover, the presence of a glide plane and strings of H-bonds (as deducted from the XRD, see section SI.5) also agrees with the simulated picture of the double columnar snowflake organization.

Both the simulation results and the X-ray diffraction analysis point to a columnar arrangement of TAA units involving many H-bonds stabilizing the structure. The alkyl tails fill the energetically unfavorable voids between the knobby "snowflake" columns, which otherwise would not form a dense phase (as found experimentally in the structure−property study where alkyl chains were shortcut[20]).

Noteworthy, the packing within the columns is quite dense: the minimal distances between the nearest-neighboring atoms from the adjacent triaryl molecules is in the range of (or even shorter than) the corresponding distances in semiconductive polycyclic aromatic hydrocarbons (Figure 4.Ie). Such dense packing can be the basis of the high electric conductivity observed experimentally in STANWs. It is certainly expected that the conductivity along the columns (Figure 4.Ie) is much higher than that in the perpendicular direction where the columnar cores are rather separated by the side alkyl chains, thus giving rise to a monodimensional transport of charges, in agreement with the conductivity behavior that was reported previously.[23]

Fibril Growth and Radical Content Evolution during Irradiation and the Follow-up Incubation in the Dark. The **TAA1** fibrils produced by a long-time white-light irradiation are remarkably well-organized and are characterized by a high radical content. The radicals are stable for a long-time after the light was switched off (*cf*. Figure 5b), while the fibrils themselves remain stable long after the radicals had decayed.[32] Below we consider a model rationalizing these findings, first, for the irradiation phase, and then for the dark phase.

Growth of Fibrils. Equations 6−8 define how the concentration c_+ of free radicals depends on the light intensity I and on the concentration c of nonaggregated TAA. eq 6 says that concentration of TAA* is $c_{A^*} \propto cI$, hence the $TAA^{\bullet+}$ production rate is proportional to cI as well eq 7. The radical annihilation rate is proportional to c_+^2 (see eq 8 noting that $TAA^{\bullet+}$ and Cl^- are paired). The two rates must be equal at equilibrium, hence

$$c_+ = k_1(cI)^{1/2},\ f_1 \equiv c_+/c = k_1(I/c)^{1/2} \qquad (9)$$

where k_1 is a constant: the fraction f_1 of nonaggregated radicals increases at low concentration of TAA.

In accordance with the established mechanisms of fibril nucleation and growth under irradiation (see Figure 4.II), the kinetic equations are

$$\frac{dm}{dt} = k_n c_+^{2n^*},\ \frac{dM}{dt} = kcm \qquad (10)$$

where m, M and $c = c_A - M$ have the same meanings as in eq 1. The first equation describes formation of the critical double-filament nuclei, $(TAA^{\bullet+})_{2n^*}$, with $n^* > 2$,[33] k_n is the corresponding nucleation rate constant. The second equation comes from eq 1 (c^* is neglected).

Equation 10 was solved in a standard way yielding the time-dependence of the number of aggregates

$$m(t) = [2/(kn^*t^*)]\tanh(t/t^*) \qquad (11)$$

the fraction of self-assembled molecules

$$w(t) \equiv M(t)/c_A = 1 - c(t)/c_A = \\ = 1 - (\cosh(tn^*/t_c))^{-2/n^*} \qquad (12)$$

and the current concentration of free radicals

$$c_+(t) = k_1(c_A I)^{1/2}\cosh\left(\frac{tn^*}{t_c}\right)^{-1/n^*} \qquad (13)$$

(*cf*. eq 9), where

$$1/t^* = \sqrt{kk_n n^*/2}\ k_1^{n^*} I^{n^*/2} c_A^{n^*/2},\ t_c = n^* t^* \qquad (14)$$

Note that the nucleation rate dm/dt decreases rapidly with time, so that $m(t) \simeq m(\infty) = 2/(kn^*t^*)$ for $t \gg t^*$.

The analogous time for concentration of free amines, $c(t)$, is longer, $\sim t_c = n^*t^*$. This means that nucleation virtually stops before the reservoir of amines is depleted, and for $t \gg t^*$ all fibrils should have roughly the same length $L(t) \simeq hN/2$ ($h \simeq 0.5$ nm, see Figure 4.IIIc), where $N \simeq M(t)/m(t)$ is the mean fibril aggregation number. It saturates at $N \simeq N_\infty = c_A/m(\infty)$ for $t \gg t_c$, where

$$N_\infty = k_1^{-n^*}\sqrt{kn^*/2k_n}\, I^{-n^*/2} c_A^{1-n^*/2} \qquad (15)$$

Thus, the nucleation stage (t^*) is always shorter than the growth stage (t_c). A lower nucleation rate constant (k_n) implies less but longer fibrils, leading to longer characteristic times t^* and t_c. A decrease of the light intensity I or of the amine concentration c_A leads to a similar effect (if $n^* > 2$). The physical origin of this effect is simple: doubling of c_A or I leads to a dramatic increase of the nucleation rate (by a factor of 8 or more), so that much more fibrils are formed, hence they have to be shorter eventually.

The number of fibrils grows nearly linearly in time, $m(t) \propto t$ for $t \lesssim t^*$, while the aggregated mass $M(t) \propto t^2$ for $t \lesssim t^*$ and $M(t) \propto t$ for $t^* \lesssim t \lesssim t_c$ (the last regime reflects the linear growth of fibril length with nearly constant number of fibrils). The NMR data on TAA solutions ($c_A = 10mM$), both classical and magic-angle NMR spectra, indicate that the aggregation time t_c is shorter than 10 min.[20]

Trapped Radicals (Irradiation Stage). Upon turning on the light, some free TAA molecules convert into free radicals (see eqs 6, 7) whose fraction rapidly rises and saturates at $f_1 = k_1(I/c)^{1/2}$ eq 9. This initial stage is not resolved by the EPR as the free radicals disappear faster than the time of one EPR measurement requiring the system to be in the dark. Therefore, in what follows we discuss only the radicals that are *trapped* in the aggregated structure (their lifetime is much longer). Their total fraction is $f = M_+/c_A$, where M_+ is the total amount of trapped radicals.

Early Irradiation Stage: Aggregation of Monomeric Radicals. As discussed above, the fibril growth (see eqs 11, 12, 15) implies trapping of some free radicals:

$$dM_+/dt = \tilde{f}(t)dM/dt \qquad (16)$$

where $\tilde{f}(t)$ is the fraction of radicals among the molecular units aggregated during dt. We adopt a natural assumption that $\tilde{f}$ is simply proportional to the fraction of free radicals, f_1, defined by the current concentration $c = c_A - M$ of free TAA:

$$\tilde{f} = k_a f_1 = k_a k_1 \sqrt{I/(c_A - M)} \qquad (17)$$

Then, by integrating eqs 16, 17 and using eq 12 we get

$$f \equiv \frac{M_+}{c_A} = f_2[1 - (\cosh(tn^*/t_c))^{-1/n^*}], \quad f_2 \equiv 2k_a k_1\sqrt{I/c_A} \qquad (18)$$

The predicted $f(t)$ grows first as $f \propto t^2$ (for $t \ll t^*$) and then as $f \propto t$ before a saturation at $t \gg t_c = n^*t^*$, where f approaches the constant f_2. The first two stages are indeed visible in the experimental data (Figure 5c): there is a very short "quadratic" stage (at $t \lesssim t^*$) followed by a roughly linear growth of f, which slows down at $t_c \sim 1$ min. However, f does not saturate at longer times (as eq 18 would suggest): rather, the linear stage is followed by a very significant regime of *nonlinear* growth where f increases by a factor of 10 (Figure 5d). A remnant of a saturation is still visible as a shoulder of the $f(t)$ plot at $t \sim 100 \div 150$ s, Figure 5c), where we also show a theoretical fit of the relevant initial part of the EPR curve using eq 18 with $n^* = 3$ (the nucleus size n^* was obtained above, *cf.* Figure 4.IIi). The fit works well up to $t \sim 100$ s and yields $t_c \approx 60$ s and $f_2 \approx 2.4\%$ for $c_A = 10$ mM (we get nearly the same t_c, but $f_2 \approx 3.2\%$ for $c_A = 1$ mM).

Intermediate Stage: Radicals Are Light-Pumped at the Fibril Ends. The observed nonlinear growth of f at $t \gtrsim t_c$ indicates that a *new* mechanism of radical formation becomes effective at longer t. The most reasonable conjecture is that the radicals are produced also among the aggregated amines (in addition to the free radicals). However, as photo-oxidation process implies an electron transfer from an amine to a solvent molecule eq 7, it seems highly improbable that it is effective for the amines buried inside STANW (the minimum distance, N to Cl, between TAA and $CHCl_3$ molecules is about 5 Å, see Figure SF10). Among all TAA units aggregated in STANW, only the *terminal* units are in close enough contact with the solvent, hence they can be converted to radical cations, Figure 6.Ia.[34] The rate of radical production (the probability that an amine unit at a given fibril end transforms to radical state in unit time) is $W_+ = k_+I$.

Let us turn to the reverse reaction of radical decay. The direct reaction

$$TAA^{\cdot+} + Cl^- \rightarrow TAA + Cl^\bullet \qquad (19)$$

is prohibited energetically. The following channel is possible, however, Figure 6.III: a *free* radical complex $TAA^{\bullet+}Cl^-$ approaches the radical at the fibril end, and they annihilate with the rate $W_- = k_-c_+$ similarly to the mechanism of eq 8, Figure 6.II.[35] The balance of the two rates

$$W_+(1-p) = W_-p \qquad (20)$$

defines the probability p of the radical state at the fibril end: $p^{-1} = k_-c_+/(k_+I) + 1$. As c_+ decreases exponentially for $t \gg t_c$ (*cf.* eq 13), the *linear* radical decay rate k_-c_+ rapidly vanishes leading to a significant growth of p. However, precisely in this regime, $t \gtrsim t_c$, another, *second*-order, radical decay reaction comes into play. This reaction channel is related to the double-columnar structure of TAA aggregates, Figure 4.III. If p is not too small, there is a significant probability (p^2) that both neighboring end-units of a double fibril are in the

radical state, so the two radicals can annihilate, Figure 6.IV. The rate of this reaction is $k_{2-}p^2$, where k_{2-} is expected to be rather small (as compared with k_-/d^3).[36] The detailed balance gives now: $W_+(1 - p) = k_{2-}p^2$ (instead of eq 20). This equation reads

$$p + (k_{2-}/k_+ l)p^2 = 1 \qquad (21)$$

It defines the probability $p = p_e$ of a radical at a column end for $t \gg t_c$. As k_{2-} is small as argued above, p_e can be high enough, so we can assume $p_e \gg f_2$ (recall that f_2 is the mean number concentration of trapped radicals in the fibrils right after their self-assembly, eq 18). The overall fraction of radicals in the system changes then to $f \approx f_2 + 4p_e/N$, where 4 stands for the number of end-amines in a double-columnar aggregate, and the total aggregation number is $N \simeq N_\infty$ for $t \gg t_c$.

Late Stage: Radicals Invade the Fibrils by Diffusion. So far we assumed that concentration of radicals inside an aggregate does not change. This is, however, not the case as the radicals can hop from one amine site to a neighbor (Figure 6.Ib); such radical hopping was observed in the literature.[37,38] The hopping process leads to radical diffusion with diffusivity $D = h^2/2t_h$, where t_h is the radical hopping time. The terminal relaxation time of this process is $t_m = L^2/(\pi^2 D)$, where $L \simeq L_\infty = hN_\infty/2$ is the fibril length. The mean fraction of radicals at a time $t > t_f$ (t_f is the effective onset time of radical formation at the fibril ends, $t_f \sim t_c$) is

$$f(t) \approx f_2 + (p_e - f_2)\,\varphi\left(\frac{t - t_f}{t_m}\right), \qquad \varphi(\tau) \equiv \frac{8}{\pi^2}\sum_{n=1,3,5\ldots}\frac{1}{n^2}(1 - e^{-\tau n^2}) \qquad (22)$$

Noting the asymptotes of φ, we predict $f - f_2 \propto (t - t_f)^{1/2}$ for $t_c \ll t \ll t_m$. The meaning of this square-root dependence is simple: The radicals created at the fibril ends diffuse inside the fibril on a distance $\Delta x \sim (D(t - t_f))^{1/2}$. The length fraction $\Delta x/L$ of the end-regions with high radical concentration ($\rho \sim \rho_e$) defines the excess amount of radicals, $f - f_2$, which is thus proportional to $(t - t_f)^{1/2}$.

The kinetics of the radical content measured in two independent EPR experiments are compared with the predictions in Figure 5d,e. A good agreement is obtained for $c_A = 10$ mM with $t_m = 1150$ s, $p_e = 0.112$. One can observe that $(f - f_2)^2$ is indeed nearly linear in time in a considerable time-window above $t_f \approx 150$ s. The EPR data thus support our model of radical kinetics.

Relaxation of Radicals (Dark Stage). From the results presented just above it is clear that after 1 h of illumination the amount of trapped radicals approaches the saturation level (*i.e.*, $f \approx p_e$). Indeed, the data shown in Figure 5d demonstrate an apparent saturation for $t > 2000$ s (note also that the best fit time parameter $t_m = 1150$ s). If the light is then switched off, the equilibrium concentration of radicals jumps to 0, $p_e \to 0$ eq 21, so the amount of radicals starts decreasing. As explained above, a radical located well inside the aggregate cannot disappear at once: it must first diffuse down to an end of the column, where the diffusive current $(D/h)\,(\partial\rho/\partial x)$ of radicals coming from the inner part of the fibril must be balanced by the end-radical decay rate $k_{2-}\rho^2$ (see the definition just above eq 21). Here $\rho(x,t)$ is the local fraction of radicals within the fibril. The corresponding diffusion process can be analyzed taking into account that all the equations can be reduced to

$$\frac{\partial y}{\partial \tau} = \frac{\partial^2 y}{\partial \xi^2};\ y(\xi,0)|_{0<\xi<\pi} = 1;\ \left.\frac{\partial y}{\partial \xi}\right|_{\xi=0} = -\left.\frac{\partial y}{\partial \xi}\right|_{\xi=\pi} = \kappa y^2 \qquad (23)$$

using the substitution $\rho(x,t) = \rho_0 y(\xi,\tau)$ with $\xi = \pi x/L$, $\tau = t/t_m$. The initial condition (at the beginning of the dark stage, $t = 0$) is $\rho(x,0) \approx \rho_0$, where $\rho_0 \approx p_e$ is defined in eq 21. Thus, the only essential parameter defining the relaxation kinetics is the reduced end-decay rate constant:

$$\kappa = k_{2-}\rho_0 Lh/(\pi D) \qquad (24)$$

An asymptotic analysis of eq 23 shows that at long times, $t \gg t_m$, the diffusion relaxation within the fibril becomes faster than the reduction at its ends, so the profile $y(\xi,\tau)$ becomes nearly uniform along the coordinate ξ. Indeed, while the terminal diffusion relaxation time τ_m is constant, the end-reduction rate κy^2 slows down significantly as the radical concentration decreases ($y \to 0$). In this regime (for late stages $t \gg t_m$, when $\langle y\rangle \lesssim \kappa^{-1}$) the asymptotic solution for the mean fraction of trapped radicals inside the fibrils, $f = \rho_0\langle y\rangle$, is

$$1/f \simeq \text{const} + 2k_{2-}(h/L)t,\ f < D/(k_{2-}Lh) \qquad (25)$$

i.e., $1/f$ increases linearly in time. This prediction is successfully verified using EPR data for several dark-stage experiments (on samples with $c_A = 1$ mM and 10 mM, with and without sonication) as demonstrated in Figure 5f. Thus, f does not tend to a finite saturation level at long times, rather it always decreases slowly as $1/t$.

For a more detailed comparison with the experiments, we solved eq 23 numerically. The calculated radical relaxation function $f(t) = \rho_0\langle y\rangle$ was compared with the EPR data for $c_A = 10$ mM in Figure 5b (here $t = 0$ corresponds to the experimental time $t_0 = 3765$ s, $\rho_0 = f_{exp}(t_0) = 0.111$). A very good agreement is obtained with

$$\kappa(10\text{ mM}) \approx 0.52,\ t_m(10\text{ mM}) \approx 1660\text{ s} \qquad (26)$$

These results allow to determine (with the error of about 10%) the reduced decay constant (which does not depend either on the fibril length or radical concentration):

$$\bar{\kappa} \equiv \frac{\kappa}{\rho_0\sqrt{t_m}} = \frac{k_{2-}h}{\sqrt{D}} \approx 0.113\ \text{s}^{-1/2} \qquad (27)$$

Note that eq 26 defines t_m, which is about 40% longer than t_m obtained in the previous section based on the radical growth data (irradiation stage). It is possible to rationalize this discrepancy: The time

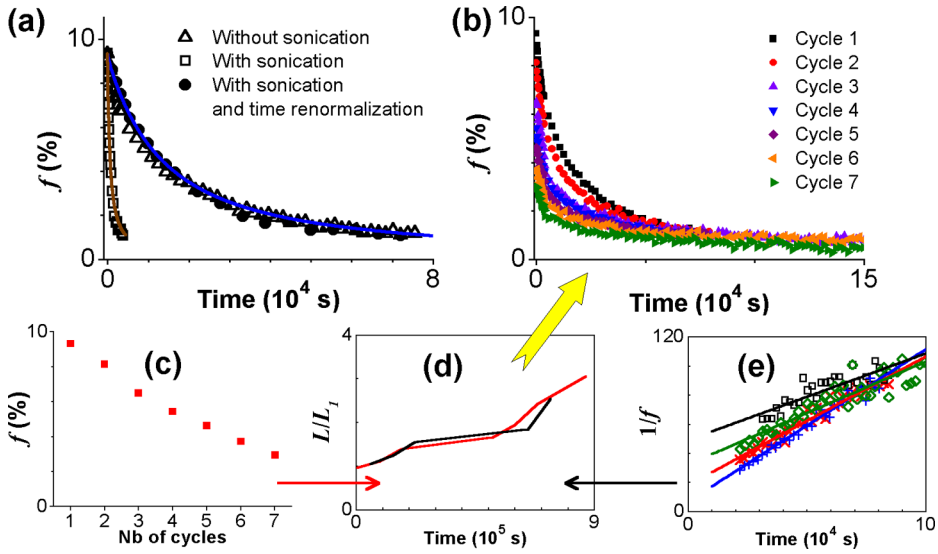

Figure 7. Radical decay in the dark in supplementary experiments highlighting the effect of fibril length: (a) The radical relaxation, *f vs* $t - t_0$, after 1 h of irradiation, $c_A = 1$ mM, $t_0 = 3765$ s, $\rho_0 = f(t_0) = 0.093$. EPR data (triangles); theory for $t_m = 3700$, $\alpha = 1.5$ (blue curve). EPR data for the same sample subjected to continuous sonication for $t > t_0$ (squares). The same data *vs* rescaled time $=18t$ (black circles). The theory for the sonicated sample with $t_m = 17$ s (brown curve). (b) The EPR data, *f vs t*, for several cycles of 1 h irradiation followed by 20 ÷ 90 h of relaxation in the dark for a TAA1 solution at $c_A = 1$ mM. The solution was monomeric before the first cycle, and the same sample was repeatedly used for each subsequent cycle. (c–e) Analysis of the data of the experiment (b): (c) The fraction of radicals *f*(0) at the end of each 1 h irradiation stage *vs* the cycle number. (d) Reduced fibril length, L/L_1 *vs* total experimental time *t*. Red curve is based on the initial fraction of radicals *f*(0) at the beginning of each dark stage: $L/L_1 \approx 0.09/f(0)$. Black curve is based on the long-time slope of 1/*f vs t*, eq 25. (e) The inverse fraction of radicals, 1/*f vs t*, for dark stages of cycles 1 (blue), 2 (red), 3 (green), 5 (black), after 1 h of irradiation in each cycle. Symbols: EPR data; lines: linear regression fits.

reported experimentally for the irradiation stage is the accumulated time during which the sample was exposed to the light. On the other hand, the very EPR measurements are taken in the dark, and this adds about 50% to real time. The diffusion relaxation of the radical distribution proceeds in real time, so the correction factor of ≈1.5 should be applied to the experimental characteristic time for the irradiation stage. By contrast, there is no such correction for the dark stage.

The EPR kinetic data for $c_A = 1$ mM (Figure 7a (triangles)) also agree very well with the predictions, eqs 23, 27, with $t_m(1\text{ mM}) \approx 3700$, implying that

$$L(1\text{ mM})/L_{\text{ref}} = (t_m(1\text{ mM})/t_m(10\text{ mM}))^{0.5} \approx 1.5 \quad (28)$$

where $L_{\text{ref}} \equiv L(10\text{ mM})$. Therefore, the fibril length increases as c_A is decreased. This is in line with our conclusion that $n^* > 2$, *i.e.*, that the critical nucleus consists of more than 4 amines eq 15.

Sonication. The analysis of eq 23 drives us to conclude that the dark-stage EPR data can be used to determine the length of supramolecular filaments with rather high precision, *cf.* eq 28. This approach is further used to find how the fibril length decreases upon sonication. The EPR data for the radical relaxation accompanied by sonication are in good agreement (Figure 7a (squares)) with the theory for $\rho_0 \approx 0.093$ and $t_m = 17$ s. The dramatic decrease of t_m on sonication can be attributed to a significantly diminished fibril length, $L \approx 0.1L_{\text{ref}}$, which therefore becomes about 15 times shorter than it was before eq 28. The consequences of sonication on more concentrated samples are similar.

Repeated Irradiation of Self-Assembled TAA Solutions. Let us turn to the EPR experiment that involves 7 cycles of 1 h irradiation (Figure 7b), each followed by relaxation in the dark during 20 ÷ 90 h. The initial number of radicals after each irradiation stage gradually decreases with the number of cycles. However, as the light intensity is constant, the saturated fraction of radicals, $f = p_e$, must be the same in all the cycles. It therefore appears that the number of radicals stays well below the saturation level for later cycles. What is the reason for this behavior? Our explanation is that a slow fibril growth becomes significant at long timescales: the fibril length increases from cycle to cycle. In fact, as we found just above, the fibril length at $c_A = 1$ mM is $L_1 \approx 1.5L_{\text{ref}}$; it corresponds to the radical diffusion time $t_m \approx 1$ h. This time is barely sufficient for the radical concentration to nearly reach the saturation level p_e along the whole fibril as a result of the first irradiation stage (which lasted 1 h). However, this is not the case any more if the fibrils are longer (*i.e.*, at the beginning of dark stages of cycles 2–7): only the end portions of the fibrils (of length $\sim L_1/2$) will be populated by the radicals after 1 h of irradiation if $L \gg L_1$. The initial *mean* fraction of radicals, f_0, at the beginning of a later dark stage (for the cycles 2–7) is therefore lower: $f_0 \sim \rho_e L_1/L$, as shown in Figure 7c. We use this equation to estimate the fibril length at the beginning at each dark

stage. The results shown in Figure 7d (red line) demonstrate that the fibril length L indeed increases with time.

To further test this idea, we analyze the long-time part of each decay curve using eq 25, which says that the slope of the dependence $1/f$ *vs* t is inversely proportional to L irrespective of the initial fraction of radicals. Some relevant plots are shown in Figure 7e (note that the data scatter more for later cycles due to a lower signal there). The obtained fibril lengths are also plotted *vs* time in Figure 7d (black line). One can observe a reasonable agreement between the two approaches yielding the fibril length time dependence. It shows that the fibril length increases roughly linearly in time. This dependence agrees with the theoretical picture of fibril growth due to the reaction rate controlled concatenation of fibrils. Another slow mechanism of fibril growth by end attachment of free TAA molecules (whose number is expected to be very low as concentration $c^* \ll c_A$) is less likely to be dominant (this mechanism leads to $L \propto \sqrt{t}$, see ref 39).

CONCLUSIONS

Although the understanding of organic supramolecular polymerization is of key importance in various domains including the design of new self-assembled materials and biomedical applications of protein fibrillization, the quantitative insight in the nature of these processes remains limited. Most of the theories do not go beyond either the simple isodesmic model[13] or the approaches developed by Asakura and Oosawa.[40] Building on the classical concepts, we have elucidated here the detailed supramolecular structure of chemically tailored triarylamines in chloroform, their self-assembly mechanisms and the kinetics of their cationic radicals stabilized in the structure. We believe that our comprehensive theoretical and experimental approaches to the radical-assisted kinetics of supramolecular polymerization can be extended to a large number of other nucleation−growth processes.

The stacked fibrillar structures in the studied amine solutions reveal the dense "snowflake" morphology (Figure 4.III) with distances between the nearest-neighboring atoms from adjacent triarylamine molecules in the range of those typical for semiconductive aromatic hydrocarbons such as pentacene. The initiation step in the nanowire formation normally requires the presence of triarylammonium radical cations generated either by light irradiation or by external oxidant (Figures 4.IIb, 3a). The radicals naturally display a nearly flat and slightly chiral conformation (in contrast to neutral free TAA molecules adopting more chiral propeller-like prismoid shape) and produce nuclei of double-columnar fibrils. The nucleation is mainly driven by dipole−dipole and $\pi-\pi$ stacking interactions of radical cations, but we found that both H-bonding and van der Waals interactions of lateral chains are also mandatory for the aggregation. It is demonstrated that all these interactions together render the growing double filaments thermodynamically stable.

Further, we established the kinetic mechanism of the radical-controlled supramolecular self-assembly of TAA molecules, which can eventually pile together up to the development of one-dimensional stacks (STANWs) revealing high metallic conductivity together with excellent stability and dynamic properties. We predict that the size of the critical nucleus to trigger the self-assembly involves $2n^* > 4$ radicals (for light, Figure 4.IIi) and $n \approx 3$ radicals (for an external oxidant, Figure 4.IVe). The strongly packed structures of double-strand fibrils and their bundles presumably serve to protect the radical cations from quenching. The nucleation step is followed by the fibril growth involving one-by-one end-attachment of neutral triarylamine molecules, which in turn change their conformation from a propeller-like prismoid to a more flat and less chiral object.

The use of light as a spatially precise and noninvasive factor is of particular interest to trigger or modify the self-assembled architectures and to design responsive materials.[41,42] We showed that, interestingly, both the fraction of radical cations (f) and the final fibril length (L) increase at lower triarylamine concentration. In addition, we established that a significant growth of the radical content in the course of light irradiation can take place long after all of the triarylamine molecules are aggregated: the characteristic time of the radical growth is much longer (by a factor of *ca*. 20 or higher) than the triarylamine aggregation time. Our analysis shows that the radical growth and decay processes occurring during the irradiation and dark stages, respectively, are caused by formation/annihilation of radicals at the fibril ends and their diffusion along the fibrils (*cf*. Figure 6). In particular, radical decomposition in the light-induced process occurs as a second order reaction due to binary contacts of radical cation/counteranion pairs. Regarding the measured metallic characteristics of STANWs,[23−25] it is likely that the radicals also serve to dope the assembled nanowires leading to their remarkably high conductivity[43] based on the revealed continuous pathways of overlapping π-orbitals along the fibril (see Figure 4.Ie). Therefore, the obtained results on the long-time radical kinetics can suggest new means to achieve and control high conductivity in organic fibrils. Recently, this new self-assembly process was used by the group of Kumar to improve the efficiency of organic solar cells.[44] Moreover, the conductivity mechanism associated with radical cations may be similar to that at work in organic stacks doped by iodine[45] or anions.[46]

Our theory of radical kinetics shows that the fraction f of radicals continuously decreases in the dark following a universal law, $f \sim 1/(t + \text{const})$ at long times, eq 25, while the fibers remain stable independently of the fraction of radicals (*i.e.*, also in the fully neutral state). The predicted kinetics are in excellent

agreement with our extensive EPR and NMR data. Thus, for the first time we obtain both qualitative and quantitative insights into the kinetics of radical cations in the self-assembling organic fibrils.

We also revealed that in addition to the nucleation and growth processes, the fraction w of aggregated molecules can increase due to a self-replication of fibrils by a tandem of scission/end-growth mechanisms (Figure 3f,g). The resultant sigmoid growth of w in TAA systems with oxidant is characterized by the growth time t_1, which is inversely proportional to the square root of the fibril scission rate defined by the oxidant concentration, and by the delay time $t_{delay} \simeq t_1 \ln(1/\gamma)$, which gets longer for lower nucleation rate (γ). The sigmoid growth is also characteristic of systems where the TAA self-assembly is triggered by a small amount of fibril seeds or by a short light pulse. These results are of interest for other self-replicating systems based on the fiber nucleation–growth processes.[47−50]

To summarize, by combining atomistic simulations with continuum statistical and kinetic models, we have uncovered the molecular structure (morphology) of TAA aggregates and provide quantitative insights into the self-assembly mechanisms and the kinetics of the radical-assisted TAA aggregation induced by light, oxidant additive or seeding, including the kinetics of the amount of stabilized cationic radicals. Our experimental and theoretical studies of the self-assembly of STANWs reveal a system with very intriguing cooperative properties strongly linking its supramolecular structure and dynamics to its function as conducting wire. Our research on the radical content and the ways to control it in the STANWs could facilitate construction of advanced functional materials with efficient electronic transport. In addition, and going further, our hierarchical approach to reveal kinetically driven nucleation–growth mechanism highlighted here, coupled to nonlinear effects emerging from self-replication phenomena, provides very general tools to study a large number of fibrillar self-assembled systems that are of first importance in material and life sciences.

METHODS

The all-atomic modeling of TAAs was performed in two stages. First, the geometry and charge distribution on isolated molecules were optimized with quantum-mechanical algorithms. Then, geometrical optimizations of molecules and their ensembles were performed using molecular mechanics algorithms. The following two analogues of **TAA1** were used in the all-atomic simulations: triphenylamine (**TAA2**) and **TAA3** (Figure 1c). The choices of the algorithms and of the model molecules are discussed in section SI.8 of the SI.

Conflict of Interest: The authors declare no competing financial interest.

Acknowledgment. The research leading to these results has received funding from the European Research Council under the European Community's Seventh Framework Program (FP7/2007-2013)/ERC Starting Grant Agreement No. 257099 (N.G.). We also thank the Agence Nationale pour la Recherche (ANR-09-BLAN-034-02) (I.N., N.J., and J.-J.C.) and the French Ministry of Research (F.N.) for fellowships. We acknowledge the Agence Nationale pour la Recherche (ANR-11-BS08-06 and ANR-11-EMMA-009), the COST action (CM1304) the University of Strasbourg (UdS), the Centre National de la Recherche Scientifique (CNRS), the international center for Frontier Research in Chemistry (icFRC), the Laboratory of Excellence for Complex Systems Chemistry (LabEx CSC), and the Institut Universitaire de France (IUF).

Supporting Information Available: Additional information on the experimental methods and details of the molecular modeling. This material is available free of charge *via* the Internet at http://pubs.acs.org.

REFERENCES AND NOTES

1. Whitesides, G. M.; Grzybowski, B. Self-Assembly at All Scales. *Science* **2002**, *295*, 2418–2421.
2. Busseron, E.; Ruff, Y.; Moulin, E.; Giuseppone, N. Supramolecular Self-Assemblies as Functional Nanomaterials. *Nanoscale* **2013**, *5*, 7098–7140.
3. Lehn, J.-M. Perspectives in Chemistry—Steps towards Complex Matter. *Angew. Chem., Int. Ed.* **2013**, *52*, 2836–2850.
4. Korevaar, P. A.; George, S. J.; Markvoort, A. J.; Smulders, M. M. J.; Hilbers, P. A. J.; Schenning, A. P. H. J.; De Greef, T. F. A.; Meijer, E. W. Pathway Complexity in Supramolecular Polymerization. *Nature* **2012**, *481*, 492–496.
5. Moulin, E.; Cormos, G.; Giuseppone, N. Dynamic Combinatorial Chemistry as a Tool for the Design of Functional Materials and Devices. *Chem. Soc. Rev.* **2012**, *41*, 1031–1049.
6. Lehn, J.-M. Toward Complex Matter: Supramolecular Chemistry and Self-Organization. *Proc. Natl. Acad. Sci. U. S. A.* **2002**, *99*, 4763–4768.
7. Aida, T.; Meijer, E. W.; Stupp, S. I. Functional Supramolecular Polymers. *Science* **2012**, *335*, 813–817.
8. Cordier, P.; Tournilac, F.; Soulié-Ziakovic, C.; Leibler, L. Self-Healing and Thermoreversible Rubber from Supramolecular Assembly. *Nature* **2008**, *451*, 977–980.
9. Jones, R. A. L. *Soft Condensed Matter*; Oxford University Press: Oxford, 2002.
10. Kleman, M.; Lavrentovich, O. D. *Soft Matter Physics: An Introduction*; Springer-Verlag: Berlin, 2003.
11. Mitov, M. *Sensitive Matter: Foams, Gels, Liquid Crystals and Other Miracles*; Harvard University Press: Cambridge, 2012.
12. Daoud, M.; Williams, C. E., Eds.; *Soft Matter Physics*; Springer-Verlag: Berlin, 1999.
13. Israelachvili, J. N. *Intermolecular and Surface Forces. With Applications to Colloidal and Biological Systems*; Academic Press Inc., Ltd.: London, 1985.
14. Hamley, I. *Introduction to Soft Matter*, 2nd ed.; John Wiley: Chichester, 2000.
15. De Gennes, P. G.; Prost, J. *The Physics of Liquid Crystals*; Clarendon: Oxford, 1993.
16. De Gennes, P.-G. *Scaling Concepts in Polymer Physics*; Cornell University Press: Ithaca, 1979.
17. Zvelindovksy, A. V., Ed.; *Nanostructured Soft Matter—Experiment, Theory, Simulation and Perspectives*; Springer: Dodrecht, 2007.
18. Davies, R. P. W.; Aggeli, A.; Beevers, A. J.; Boden, N.; Carrick, L. M.; Fishwick, C. W. G.; McLeish, T. C. B.; Nyrkova, I.; Semenov, A. N. Self-Assembling Beta-Sheet Tape Forming Peptides. *Supramol. Chem.* **2006**, *18*, 435–443.
19. Nyrkova, I. A.; Semenov, A. N. Theory of Chiral Recognition in DNA Condensation. *Soft Matter* **2009**, *5*, 979–989.
20. Moulin, E.; Niess, F.; Maaloum, M.; Buhler, E.; Nyrkova, I.; Giuseppone, N. The Hierarchical Self-Assembly of Charge

Nanocarriers: A Highly Cooperative Process Promoted by Visible Light. *Angew. Chem., Int. Ed.* **2010**, *49*, 6974–6978.
21. Moulin, E.; Niess, F.; Jouault, N.; Buhler, E.; Giuseppone, N. Light-Triggered Self-Assembly of Triarylamine-Based Nanospheres. *Nanoscale* **2012**, *4*, 6748–6751.
22. Giuseppone, N. Toward Self-Constructing Materials: A Systems Chemistry Approach. *Acc. Chem. Res.* **2012**, *45*, 2178–2188.
23. Faramarzi, V.; Niess, F.; Moulin, E.; Maaloum, M.; Dayen, J.-F.; Beaufrand, J.-B.; Zanettini, S.; Doudin, B.; Giuseppone, N. Light-Triggered Self-Construction of Supramolecular Organic Nanowires as Metallic Interconnects. *Nat. Chem.* **2012**, *4*, 485–490.
24. Moulin, E.; Martin, J.-J.; Giuseppone, N. Advances in Supramolecular Electronics—From Randomly Self-assembled Nanostructures to Addressable Self-Organized Interconnects. *Adv. Mater.* **2013**, *25*, 477–487.
25. Armao, J. J.; Maaloum, M.; Ellis, T.; Fuks, G.; Rawiso, M.; Moulin, E.; Giuseppone, N. Healable Supramolecular Polymers as Organic Metals. *J. Am. Chem. Soc.* **2014**, 10.1021/ja5044006.
26. Here and below k_BT is the thermal energy corresponding to the ambient temperature of 293 K, 1 kcal/mol = 1.72k_BT. The effective dielectric constant was chosen to be $\varepsilon = 2.2$.
27. The solvation energy contribution is taken into account both in the dissociation energy E_{ca} and in the fibril end-association energy E_{as}.
28. More precisely, it is the bonds between CT dimers and the neighboring neutral TAA molecules that serve as weak points of the columnar structure (see green dashed lines in Figure 3g).
29. Amthor, S.; Noller, B.; Lambert, C. UV/Vis/NIR Spectral Properties of Triarylamines and their Corresponding Radical Cations. *Chem. Phys.* **2005**, *316*, 141–152.
30. Fitzgerald, E. A.; Wuelfing, P.; Richtol, H. H. Photochemical Oxidation of Some Substituted Aromatic Amines in Chloroform. *J. Phys. Chem.* **1971**, *75*, 2737–2741.
31. The period is doubled due to different orientations of L- and D-molecules alternating along the "snowflake" column. By contrast, the period is h = 0.5 nm in the "Mercedes-Benz" pattern, as all the molecules have the same twirl there.
32. An EPR experiment after 4 weeks of radical decay in the dark revealed full disappearance of the spins. However, the NMR spectrum of the same sample still showed the flattening of the aromatic resonance signals evidencing that the columnar assembly is maintained independently of the radicals, which therefore act just as kinetic triggers for the self-assembly.
33. The critical nucleus size n^* may depend also on solution concentration c; however, this dependence is expected to be weak.[51−54] Further, the nucleus may consist of both the radicals and normal amines.
34. Actually, this conversion may be even easier here than in the case of free TAA molecules, since aggregated TAA units already adopt a flat conformation, which is more favorable for radical formation.
35. Note that a similar decay mechanism is prohibited for $TAA^{\bullet+}$ radicals trapped inside the fibril (with Cl^- located at the fibril edge) due to a necessarily large distance between the cation and the Cl^- counterion (Figure SF10).
36. For the following reasons: (a) The activation reaction, Figure 6.IVa, is more difficult here since the resultant neutral TAA molecules at the fibril edge are forced to be in a flat conformation, which favors the radical state. (b) The transient radical $Cl^{\bullet}$ has to travel a significant distance $\sim d \sim$ 10 Å in order to meet the chloride anion, Figure 6.IVb.
37. Low, P. J.; Paterson, M. A. J.; Puschmann, H.; Goeta, A. E.; Howard, J. A. K.; Lambert, C.; Cherryman, J. C.; Tackley, D. R.; Leeming, S.; Brown, B. Crystal, Molecular and Electronic structure of N,N′-diphenyl-N,N′-bis(2,4-dimethylphenyl)-(1,1′-biphenyl)-4,4′-diamine and the Corresponding Radical Cation. *Chem.—Eur. J.* **2004**, *10*, 83–91.
38. Lambert, C.; Nöll, G.; Schelter, J. Bridge-Mediated Hopping or Superexchange Electron-Transfer Processes in Bis-(triarylamine) Systems. *Nat. Mater.* **2002**, *1*, 69–73.
39. Semenov, A. N.; Nyrkova, I. A. End Growth/Evaporation Living Polymerization Kinetics Revisited. *J. Chem. Phys.* **2011**, *134*, 114902.
40. Oosawa, F.; Asakura, S. *Thermodynamics of the Polymerization of Protein*; Academic Press: San Diego, 1975.
41. Jochum, F. D.; Theato, P. Temperature- and Light-Responsive Smart Polymer Materials. *Chem. Soc. Rev.* **2013**, *42*, 7468–7483.
42. Burnworth, M.; Tang, L.; Kumpfer, J. R.; Duncan, A. J.; Beyer, F. L.; Fiore, G. L.; Rowan, S. J.; Weder, C. Optically Healable Supramolecular Polymers. *Nature* **2011**, *472*, 334–338.
43. Akande, A.; Bhattacharya, S.; Cathcart, T.; Sanvito, S. First Principles Study of the Structural, Electronic, and Transport Properties of Triarylamine-Based Nanowires. *J. Chem. Phys.* **2014**, *140*, 074301.
44. Kumar, R. H.; Churches, Q. I.; Subbiah, J.; Gupta, A.; Ali, A.; Evaus, R. A.; Holmes, A. B. Enhanced Photovoltaic Efficiency *via* Light-Triggered Self-Assembly. *Chem. Commun.* **2013**, *49*, 6552–6554.
45. Prasanthkumar, S.; Gopal, A.; Ajayaghosh, A. Self-Assembly of Thienylenevinylene Molecular Wires to Semiconducting Gels with Doped Metallic Conductivity. *J. Am. Chem. Soc.* **2010**, *132*, 13206–13207.
46. Vernitskaya, T. V.; Efimov, O. N. Polypyrrole: a Conducting Polymer: Its Synthesis, Properties and Applications. *Russ. Chem. Rev.* **1997**, *66*, 489–505.
47. Patzke, V.; Von Kiedrowski, G. Self Replicating Systems. *ARKIVOC* **2007**, *338*, 293–310.
48. Nguyen, R.; Allouche, L.; Buhler, E.; Giuseppone, N. Dynamic Combinatorial Evolution within Self-Replicating Supramolecular Assemblies. *Angew. Chem., Int. Ed.* **2009**, *48*, 1093–1096.
49. Bissette, A. J.; Fletcher, S. P. Mechanisms of Autocatalysis. *Angew. Chem., Int. Ed.* **2013**, *52*, 12800–12826.
50. Takahashi, Y.; Mihara, H. Construction of a Chemically and Conformationally Self-Replicating System of Amyloid-Like Fibrils. *Bioorg. Med. Chem.* **2004**, *12*, 693–699.
51. Nyrkova, I. A.; Semenov, A. N. Multimerization: Closed or Open Association Scenario? *Eur. Phys. J. E: Soft Matter Biol. Phys.* **2005**, *17*, 327–337.
52. Nyrkova, I. A.; Semenov, A. N.; Aggeli, A.; Boden, N. Fibril Stability in Solutions of Twisted Beta-Sheet Peptides: A New Kind of Micellization in Chiral Systems. *Eur. Phys. J. B* **2000**, *17*, 481–497.
53. Nyrkova, I. A.; Semenov, A. N. On the Theory of Aggregation and Micellization: PEO-PVP Copolymer in Water. *Faraday Discuss.* **2005**, *128*, 113–127.
54. Nyrkova, I. A.; Semenov, A. N. On the Theory of Micellization Kinetics. *Macromol. Theory Simul.* **2005**, *14*, 569–585.